Control of droplet evaporation on smooth chemical patterns

PHYSICAL REVIEW FLUIDS **00**, 003900 (2021)

Control of droplet evaporation on smooth chemical patterns

Michael Ewetola,[1] Rodrigo Ledesma-Aguilar,[2] and Marc Pradas[1,*]

[1]*School of Mathematics and Statistics, The Open University, Milton Keynes MK7 6AA, United Kingdom*

[2]*Institute for Multiscale Thermofluids, School of Engineering, University of Edinburgh, The King's Buildings, Mayfield Road, Edinburgh EH9 3FB, United Kingdom*

(Received 5 September 2020; accepted 26 February 2021; published xxxxxxxxxx)

We investigate the evaporation of a two-dimensional droplet on a solid surface. The solid is flat but with smooth chemical variations that lead to a space-dependent local contact angle. We perform a detailed bifurcation analysis of the equilibrium properties of the droplet as its size is changed, observing the emergence of a hierarchy of bifurcations that strongly depends on the particular underlying chemical pattern. Symmetric and periodic patterns lead to a sequence of pitchfork and saddle-node bifurcations that make stable solutions become saddle nodes. Under dynamic conditions, this change in stability suggests that any perturbation in the system can make the droplet shift laterally while relaxing to the nearest stable point, as is confirmed by numerical computations of the Cahn-Hilliard and Navier-Stokes system of equations. We also consider patterns with an amplitude gradient that creates a set of disconnected stable branches in the solution space, leading to a continuous change of the droplet's location upon evaporation.

DOI: 10.1103/PhysRevFluids.00.003900

I. INTRODUCTION

The ability to control the configuration of a droplet evaporating on a solid surface is important for a wide range of applications, such as printing, coating, micropatterning, and heat transfer [1]. One of the key issues is to understand how the properties of the solid affect the contact line of the droplet, i.e., the line where all phases meet, and a substantial amount of work has been dedicated to that matter; see, e.g., Refs. [2–10]. In the ideal limit of a perfectly smooth and flat solid surface, a droplet keeps a constant shape characterized by the intersection angle of the liquid-gas interface with the solid. Such a constant-contact-angle mode of evaporation implies the smooth retraction of the contact line as the droplet evaporates.

In contrast, surfaces with microscopic defects, either chemical or topographical, are able to induce the phenomenon known as contact-line pinning, whereby the translational motion of the contact line is suppressed [2]. Therefore, in the limiting situation of complete pinning, an evaporating droplet would exhibit a constant-contact-area mode of evaporation. In practice, a widely accepted view is that droplet evaporation proceeds either as a combination of these two limiting modes, often called a stick-slip mode of evaporation [6], or as a combination of pinning and depinning of the contact line, called a stick-jump mode [7].

Recently, ultrasmooth smooth pinning-free surfaces which allow large-scale wettability patterns (comparable to the droplet size) have been developed. Such surfaces can be achieved by introducing an intermediary smooth layer that shields the droplet from the underlying solid surface and include Slippery Liquid Infused Porous Surfaces (SLIPSs) [11–13] and Slippery Covalently Attached Liquid Surfaces (SOCALSs) [14]. On flat SLIPSs and SOCALSs, a constant-contact-angle mode of

*marc.pradas@open.ac.uk

evaporation has been reported, supporting the absence of contact-line pinning on these surfaces [15,16]. However, introducing a large-scale topographical patterning has been shown to induce bifurcations between well-defined droplet configurations upon evaporation, which are paced by dynamic snap events [17]. This has opened up the possibility to use solid surfaces with smooth wettability variations to control both the evaporation process and the motion of the droplet.

Here we build on the ideas presented in Ref. [17] for nonplanar surfaces to study the evaporation of two-dimensional (2D) droplets on a perfectly flat and smooth but chemically patterned surface. We consider chemical patterns that lead to a smooth variation of the local equilibrium contact angle, thus eliminating pinning effects that may arise as a consequence of sharp discontinuities. Such smooth variation of the chemical pattern occurs over a typical length scale λ which we assume to be comparable to the droplet footprint. This limit is particularly relevant for applications as this type of surface is easier to implement experimentally. While chemical patterning typically leads to pinning points on a solid surface, recent progress has been made in creating liquid-like surfaces [18] and liquid-infused surfaces [19] with very low pinning. Such surfaces could be used to study a continuous variation of the surface wettability as an experimental system to explore the ideas presented in this paper.

The evaporation is assumed to be quasistatic and dictated by the equilibrium properties of the system, which depend on both the droplet's size and the specific chemical pattern of the substrate. By constructing the interfacial energy landscape of the system, we identify all possible equilibrium solutions of the droplet shape. On perfectly symmetric patterns, equilibrium solutions correspond to branches parametrized by the droplet's cross-sectional area, position, and contact radius. Such branches form a network in the three-dimensional (3D) parameter space, where nodes correspond to pitchfork bifurcation points. Increasing the amplitude of the wettability pattern gives rise to folded nodes that signal the onset of saddle-node bifurcations. Introducing a weak bias in the pattern leads to a disconnection of the equilibrium branches and to the symmetry breaking of the pitchfork bifurcation nodes. Increasing the strength of the bias creates a set of continuous branches of stable equilibrium solutions where the droplet's position varies smoothly upon changes in the cross-sectional area, suggesting that directed motion is possible on this type of surfaces.

To understand the droplet dynamics upon evaporation on chemically patterned surfaces, we present numerical simulations of the Cahn-Hilliard and Navier-Stokes system of equations. We focus on the quasistatic regime, where droplet evaporation is dominated by diffusion into the gas phase. For periodic and symmetric patterns, the droplet exhibits lateral movements when its cross-sectional area reaches the pitchfork bifurcations predicted by the theory, equivalent to the snap evaporation mode reported by Wells *et al.* [17] on nonplanar surfaces. On asymmetric patterns, the pitchfork branches are disconnected, and the droplet follows a smooth motion in a preferred direction as its size decreases in time, also in good agreement with the theory. Our results show that the interplay between a phase change and surface wettability can be exploited to control the motion of droplets on patterned solid surfaces in the absence of the anchoring effect of pinning.

II. EQUILIBRIUM PROPERTIES: BIFURCATION ANALYSIS

Figure 1(a) shows a schematic representation of the system considered in this work. A 2D droplet rests on a solid flat surface of nonuniform wettability. Here we consider a periodic variation of the surface chemical properties along the lateral coordinate, x, which we model using a spatially dependent function, $\Theta(x)$, given by

$$\cos\Theta(x) = \cos\theta_0 - \epsilon\mathcal{F}(x), \tag{1}$$

where θ_0 is the reference homogeneous contact angle, ϵ controls the strength of the chemical pattern, and $\mathcal{F}(x)$ is a generic periodic function. [We note that the reason to write $\cos\Theta(x)$ in the above equation is to simplify the analytical treatment presented below; see Eq. (3)].

We assume that the function $\mathcal{F}(x)$ varies smoothly over a length scale λ without sharp discontinuities, hence ruling out the presence of pinning effects. Consequently, at equilibrium, and

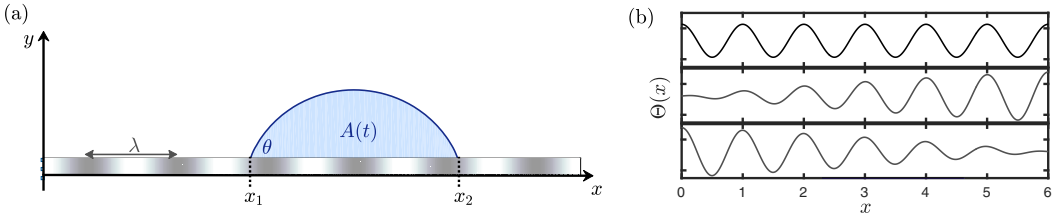

FIG. 1. (a) 2D droplet on a flat substrate with a smoothly varying chemical pattern. The location of the droplet's contact points is x_1 and x_2, and the contact angle is θ. The droplet size $A(t)$ decreases in time, and λ is the wavelength of the periodic pattern. (b) Examples of chemical patterns, which are described by the local contact angle $\Theta(x)$.

in the absence of gravity, the contact angle θ on both contact points of the droplet, x_1 and x_2, is the same and equal to the contact angle imposed by the chemical pattern, i.e., $\theta = \Theta(\ell \pm R)$. Here, $\ell = (x_1 + x_2)/2$ is the droplet shift and corresponds to the location of the droplet's midpoint relative to the origin $x = 0$, and $R = (x_2 - x_1)/2$ is the droplet footprint; see Fig. 1. Therefore, the shape of the free surface of the droplet, which we denote as $h(x)$, is given by a circular arc whose cross-sectional area A satisfies the relation

$$A = \frac{R^2}{2}\frac{2\theta - \sin(2\theta)}{\sin^2\theta}, \tag{2a}$$

$$\cos\theta = \cos\theta_0 - \epsilon\mathcal{F}(\ell \pm R). \tag{2b}$$

For a fixed droplet area, the stability of the equilibrium solutions for (ℓ, R) that satisfy Eqs. (2) can be determined from the interfacial energy (per unit length of the contact line)

$$E(\ell, R) = \frac{2\gamma\theta R}{\sin\theta} - \gamma\int_{\ell-R}^{\ell+R}\cos\Theta(x)\,dx, \tag{3}$$

where γ is the liquid/gas surface tension. Inserting Eq. (1) into Eq. (3) gives

$$E(\ell, R) = 2\gamma R\left(\frac{\theta}{\sin\theta} - \cos\theta_0\right) + \gamma\int_{\ell-R}^{\ell+R}\epsilon\mathcal{F}(x)\,dx, \tag{4}$$

where R and θ are given by Eqs. (2). For a given droplet's area A, we can compute the interfacial energy and find its extrema, which correspond to the equilibrium states of the droplet. In the following, we will analyze how the stability of the equilibrium states changes with the droplet area, leading to a hierarchy of bifurcation diagrams that are dictated by the underlying chemical pattern. These bifurcation diagrams will, in turn, inform about the possible (stable) trajectories in the (A, ℓ, R) space, which can be observed as the droplet's size is dynamically changed; see Sec. III B.

A. Periodic and symmetric chemical patterns

We start by considering periodic and symmetric patterns. For simplicity, we consider the function $\mathcal{F}(x) = \cos(kx)$, where $k = 2\pi/\lambda$ and λ is the wavelength of the chemical variation. We nondimensionalize the system of Eqs. (2) and (4) by taking λ as the typical length scale, such that the new dimensionless variables are $x' = x/\lambda$, $R' = R/\lambda$, $A' = A/\lambda^2$, and $E' = E/(\gamma\lambda)$. For convenience, we will drop the primes in the notation used in the rest of the paper. Under these conditions, Eq. (4) becomes

$$E(\ell, R) = 2R\left(\frac{\theta}{\sin\theta} - \cos\theta_0\right) + \frac{\epsilon}{\pi}\sin(2\pi R)\cos(2\pi\ell), \tag{5}$$

where θ and R are related through Eqs. (2).

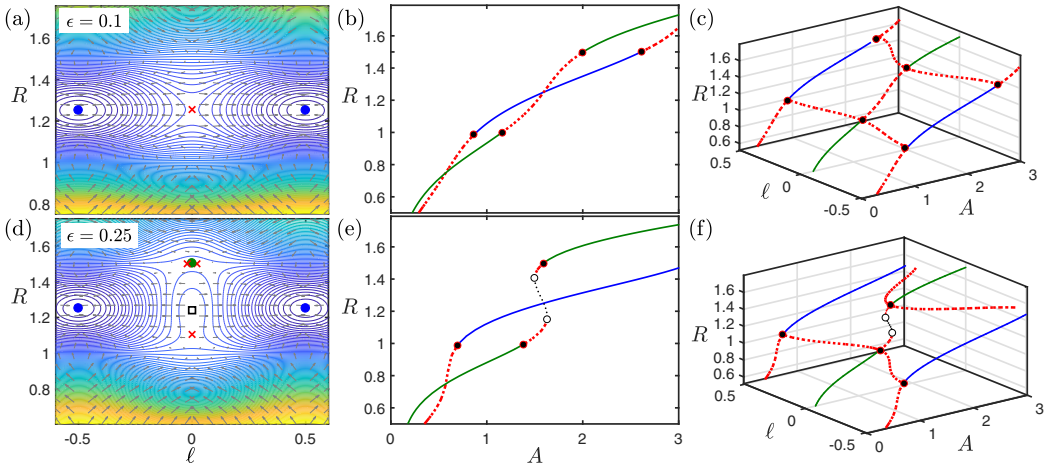

FIG. 2. Top panels (a), (b), (c) correspond to $\epsilon = 0.1$ and lower panels (d), (e), (f) to $\epsilon = 0.25$. (a), (d) Interfacial energy contour plots for $A = 1.5$, where energy levels increase from blue to yellow. Blue and green circles correspond to stable equilibrium solutions, crosses to saddle nodes that are stable to axisymmetric perturbations but unstable against lateral displacements, and empty squares to unstable solutions. (b), (e) Droplet lateral radius R as function of the area A, where green and blue branches correspond to droplet stable solutions that are aligned with a maximum and a minimum of the chemical pattern, respectively. The red dashed branches are saddle nodes, and the black dotted branch corresponds to unstable solutions. (c), (f) Bifurcation diagrams showing all possible solutions. Solid points represent subcritical pitchfork bifurcations, and empty circles mark the onset of saddle-node bifurcations. In all cases $\theta_0 = 70^\circ$.

We will now show that depending on the strength of variation of the chemical pattern, given by the amplitude ϵ, different bifurcation points emerge as the droplet's size is changed.

1. Pitchfork bifurcation

We first consider relatively small values of ϵ. We note that the work done in Ref. [20] analyzed this case with a chemical pattern given by $\Theta(x) = \theta_0 + \epsilon \cos(kx)$, reporting the emergence of subcritical pitchfork bifurcations on the (ℓ, A) diagram. In this section, we revisit this case with the chemical pattern given by Eq. (2b), which has the advantage that it leads to the explicit expression of the energy, Eq. (5).

Figure 2(a) shows a contour plot of the energy for a fixed droplet size, $A = 1.5$, and for $\epsilon = 0.1$. We first focus on equilibrium solutions for the droplet shape aligned with minima and maxima of the chemical pattern, marked with blue circles and red crosses in the figure. Solutions that are aligned with a minimum of the chemical pattern [i.e., $\ell = \pm(2n + 1)/2$ for $n = 0, 1, 2, \dots$] are stable, whereas solutions that are aligned with a maximum ($\ell = \pm n$ for $n = 0, 1, 2, \dots$) are saddle nodes, which are stable to axisymmetric perturbations but unstable against lateral displacements along the solid surface. Therefore, if the droplet is on a saddle node, any perturbation on the system will destabilize the droplet's location and make the droplet shift laterally to either of the two stable solutions that are located to the left or right [20].

By fixing the location of the droplet to be aligned with either a maximum or minimum of the chemical pattern, and by changing the droplet size A, we construct two branches of solutions that are parametrized by the droplet's lateral radius R, as shown in Fig. 2(b), where dashed lines correspond to saddle nodes and solid lines correspond to stable solutions. The stability of these solutions changes from stable to saddle node (or vice versa) at specific values of A. Extending this analysis to include droplet solutions that are located between minima and maxima of the chemical pattern yields the 3D bifurcation diagram shown in Fig. 2(c). Stability transitions correspond to

pitchfork bifurcations: a stable point (green solid line) collides with two saddle nodes to become a saddle node (subcritical pitchfork bifurcation), and a saddle node collides with two saddle nodes to become a stable solution (inverted subcritical pitchfork bifurcation). Therefore, in a dynamic situation, where the droplet's area is slowly decreasing in time, it is expected that around these bifurcation points, any perturbation that can break the plane symmetry will make the droplet shift and change location: if it is aligned with a maximum of the chemical pattern, it will move to a minimum and vice versa.

The critical droplet footprint R_{p} at which the pitchfork bifurcations occur can be determined explicitly by noting that at these points the stability of the solution changes from a stable to a saddle node. Hence, these points satisfy $\partial_\ell^2 E(\ell, R_{\mathrm{p}}) = 0$. Imposing this condition to Eq. (5) gives the relation

$$\sin(2\pi R_{\mathrm{p}}) = 0, \tag{6}$$

and hence the pitchfork critical radii are

$$R_{\mathrm{p}} = \frac{n}{2}, \tag{7}$$

for $n = 1, 2, \ldots$. Therefore, pitchfork bifurcations occur at precise locations of the droplet's edges: at either minima or maxima of the chemical pattern. Remarkably, this geometrical property holds regardless of the chemical pattern, i.e., R_p is independent of the homogeneous contact angle, θ_0, and the amplitude of the substrate's chemical variation, ϵ. Instead, the effect of these parameters is to determine the critical contact angle θ_{p} and area A_{p} at the bifurcation points, which follow from Eq. (2).

2. Cusp and saddle-node bifurcations

For larger values of ϵ, we observe multiple solutions for the same droplet area and midpoint location [see green circle, empty box, and red cross at $\ell = 0$ in Fig. 2(d)]. Such solutions lie within S-shaped branches of the $R(A)$ curve characterized by two turning points [see Fig. 2(e)]. These turning points mark the onset of saddle-node bifurcations whereby a saddle node solution collides with an unstable solution. Such transitions are identified as empty circles in the 3D bifurcation diagram shown in Fig. 2(f).

The emergence of unstable solutions is a consequence of a cusp bifurcation that occurs as ϵ is continuously increased, as is shown in Fig. 3(a). At the critical cusp point, ϵ_c, two new branches of solutions emerge, which correspond to the two turning points. Figures 3(b) and 3(c) show the evolution of these turning points on the (ϵ, A) and (ϵ, R) planes, in agreement with the standard form of the cusp bifurcation [21].

It is important to note that the saddle-node bifurcations (i.e., the turning points on the $R(A)$ curve) are observed not only as ϵ increases, but also as the droplet size A increases for a fixed value of ϵ, as is shown in Fig. 3(d). We can understand this set of folds as a result of a series of cusp bifurcations that occur at different critical points in the (ϵ, A, R) space; i.e., each cusp bifurcation is described in terms of a critical strength ϵ_c, a critical size A_c, and critical radius R_c.

Figure 3(e) shows the set of critical amplitudes ϵ_c as a function of the critical droplet size A_c. To understand the scaling relation between ϵ_c and A_c, we note that for a fixed ℓ, the turning points in Fig. 3(d) are given by the stationary points of the function $A(R)$, i.e., $dA/dR = 0$, where $A(R)$ is given by Eq. (2). In the limit of $\epsilon \to 0$ we write the expansion

$$A = A_0(R)\left[1 + \frac{\epsilon}{\beta}\cos(2\pi R)\right] + \text{h.o.t}, \tag{8}$$

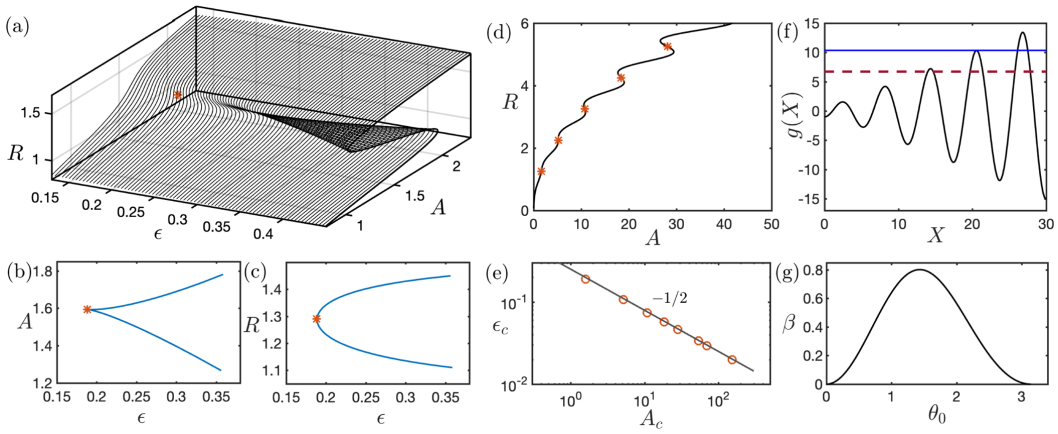

FIG. 3. (a), (b), (c) Emergence of a cusp bifurcation as the strength of the chemical pattern, ϵ, is increased for the case with $\theta_0 = 70^\circ$. Panel (a) shows the 3D plot (ϵ, A, R), where the red asterisk marks the critical cusp point. Panels (b) and (c) show the corresponding projections onto the (ϵ, A) and (ϵ, R) planes, respectively. (d) Droplet footprint as function of its size for $\epsilon = 0.1$ and $\ell = 0$. Red asterisk mark the critical radii at which a cusp bifurcation occurs. (e) Critical values of the strength of the chemical pattern to induce a cusp bifurcation as function of the droplet size. Solid line corresponds to a power law with exponent $-1/2$. (f) Plot of the function $g(X)$ where solid and dashed lines correspond to β/ϵ with $\theta_0 = 70^\circ$ and $\epsilon = 0.046$ and $\epsilon = 0.058$, respectively. (g) Plot of the function $\beta(\theta_0)$.

where $A_0 = R^2(2\theta_0 - \sin(2\theta_0)/2\sin^2\theta_0$ is the droplet size when $\epsilon = 0$, and we have defined the parameter

$$\beta = \frac{(\theta_0 - \sin\theta_0\cos\theta_0)\sin\theta_0}{2(1 - \theta_0\cot\theta_0)}. \tag{9}$$

Imposing $dA/dR = 0$ in Eq. (8) and rearranging we find that the radii R_s at which the saddle-node bifurcations occur are solutions of the transcendental equation

$$\frac{X_s}{2}\sin X_s - \cos X_s = \frac{\beta(\theta_0)}{\epsilon}, \tag{10}$$

where $X_s = 2\pi R_s$. In addition, we note that the stationary points X_c of the function

$$g(X) = \frac{X}{2}\sin X - \cos X \tag{11}$$

correspond to the onset of the cusp bifurcation. Therefore, the critical value ϵ_c where the cusp bifurcation occurs can be obtained by imposing the condition $g(X_c) = \beta/\epsilon_c$.

Figure 3(f) shows a plot of the function $g(X)$ and the constant β/ϵ for $\theta_0 = 70^\circ$ and two arbitrary values of ϵ. For $\epsilon = 0.046$ the plot shows a cusp bifurcation that corresponds to the first intersection between the constant β/ϵ (blue solid line) and the function $g(X)$ at the maximum $X_c \approx 20$. Increasing the amplitude of the chemical pattern to $\epsilon = 0.058$ around $X = 20$, the constant β/ϵ (red dashed line) intersects $g(X)$ at two points that correspond to the saddle node bifurcations.

Expanding the function $g(X)$ around X_c, we find that the solutions near the cusp bifurcation are given by

$$X \simeq X_c \pm \delta\left(\frac{1}{\epsilon} - \frac{1}{\epsilon_c}\right)^{1/2}, \tag{12}$$

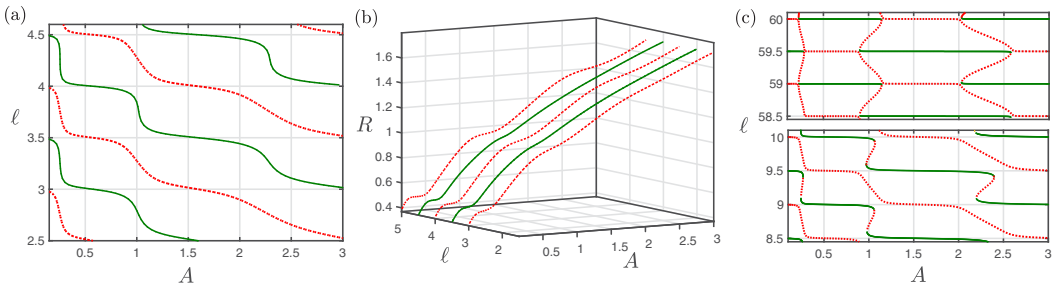

FIG. 4. Bifurcation diagrams for the case of a chemical pattern with an amplitude gradient, given by Eq. (14) with $\epsilon = 0.1$ and $L = 6$. Panel (a) shows the equilibrium solutions of the droplet's midpoint location, ℓ, as function of its size A, and panel (b) the bifurcation diagram in the 3D space (A, ℓ, R). Solid green lines correspond to stable solutions, and dashed red lines correspond to saddle nodes. Panel (c) shows the bifurcation diagram on the (A, ℓ) plane when $\ell > L$ (bottom) and $\ell \gg L$ (top). In all cases $\theta_0 = 70^\circ$.

where $\delta = \sqrt{2\beta(\theta_0)/g''(X_c)}$ is a constant that depends on θ_0 only, and the critical value is given by

$$\epsilon_c = \frac{\beta(\theta_0)}{g(X_c)} \sim \beta(\theta_0) A_c^{-1/2}, \tag{13}$$

where we have approximated $g(X_c) \sim X_c/2$, transformed back to the radius variable R, and made use of the fact that at the onset of the cusp bifurcation $A \sim R^2$. The above relation is in agreement with the scaling behavior shown in Fig. 3(e). Because β is always finite [cf. 3(g)], an important conclusion is that cusp, and, consequently saddle node bifurcations are observed for any wetting condition, as long as $\epsilon \neq 0$. In addition, because the critical cusp area A_c is normalized by the squared wavelength λ^2, we conclude that, for a fixed droplet area, cusp bifurcations are favored in the microscopic limit of $\lambda \to 0$.

B. Patterns with an amplitude gradient

The results shown in Fig. 2 indicate that, on symmetric chemical patterns, a droplet will adopt equilibrium configurations which are aligned with either a maximum or a minimum of the pattern. As the droplet's size changes, the stability of such configurations alternates between stable and saddle nodes through a sequence of pitchfork bifurcations that can promote droplet lateral motion: any perturbation that breaks the plane symmetry will make the droplet change from a saddle node to a stable location where the interfacial energy is at a minimum. However, and because of symmetry, there is no bias for the change in position of the droplet, hence ruling out the possibility to induce droplet motion towards a *preferred* direction. To this end, here we explore a nonsymmetrical chemical pattern with the aim to determine whether it is possible to achieve directed displacement in the droplet's location as the droplet size is changed.

We consider a pattern with an amplitude gradient described by the function

$$\mathcal{F}(x) = \frac{2}{\pi} \arctan\left(\frac{x}{L}\right) \cos(2\pi x), \tag{14}$$

where L is the length over which the gradient varies. An example of the above pattern with $\epsilon = 0.2$ and $L = 6$ is shown in Fig. 1(b). (We note that the change of sign of the gradient can be imposed by replacing x by $L - x$ in the argument of the arctan.)

We solve Eqs. (2) alongside Eq. (14) to find the equilibrium solutions for a given droplet size. Following the same procedure as in the previous section, we construct the bifurcation diagrams as the droplet size is changed. Figure 4 shows the branches of solutions on the (A, ℓ) plane and in the (A, ℓ, R) space. We observe that the lack of symmetry of the chemical pattern leads to a topological change in the bifurcation diagrams, characterized by a series of disconnected branches, which are

either stable or saddle node. In particular, we can see that as the droplet size is changed, there always exists a set of stable branches that can be continuously parametrized by the droplet's midpoint, i.e., $\ell(A)$. This implies that changing the droplet size can lead to a continuous lateral displacement along a preferred direction.

To understand the onset of symmetry breaking and the consequent topological change in the bifurcation diagram, let us focus on the case of $\ell > L$, noting that in the limit of $\ell \gg L$, the chemical pattern given by Eq. (14) becomes symmetric and equivalent to the case considered in the previous section. The bottom panel of Fig. 4(c) shows the emergence of turning points along the stable branches for $\ell > L$, which in the limit of $\ell \gg L$ (top panel) become pitchfork bifurcation points, thereby connecting the two previously disconnected stable and saddle node branches. This shows how the topological change in the bifurcation diagrams is purely controlled by the degree of asymmetry of the chemical pattern.

III. DROPLET EVAPORATION

In this section we study the evaporation of a 2D droplet on a solid surface. We assume that evaporation is quasistatic and driven by mass diffusion in the gas phase; hence, we neglect the effect of a temperature difference between the solid, liquid, and gas phases. To model such a system, we adopt a diffuse-interface formulation that includes a wetting boundary condition at the solid substrate as well as an open boundary to drive the evaporation of the droplet.

A. Diffuse-interface formulation

We consider the Cahn-Hilliard and Navier-Stokes (CH-NS) system of equations for an incompressible fluid:

$$\frac{\partial \phi}{\partial t} + \mathbf{u}\cdot\nabla\phi = M\nabla^2\eta(\phi), \tag{15a}$$

$$\rho\left[\frac{\partial \mathbf{u}}{\partial t} + (\mathbf{u}\cdot\nabla)\mathbf{u}\right] = -\nabla p + \mu\nabla^2\mathbf{u} - \phi\nabla\eta, \tag{15b}$$

$$\nabla\cdot\mathbf{u} = 0, \tag{15c}$$

where $\mathbf{u}$ is the velocity field, p is the pressure, ρ the density, μ the dynamic viscosity, and M the mobility parameter. The above equations are integrated in a 2D domain Ω with boundary $\partial\Omega$, where ϕ is a locally conserved field that plays the role of an order parameter by taking two equilibrium limiting values, $\phi = +\phi_e$ and $\phi = -\phi_e$, which represent the liquid and vapor phases, respectively. Hence, in the following we identify the location of the interface as the level curve $\phi = 0$.

We define the chemical potential field, $\eta = \delta\mathcal{F}[\phi]/\delta\phi$, where $\mathcal{F}$ is the free energy of the system:

$$\mathcal{F}[\phi] = \int_\Omega \frac{\sigma}{\xi}\left[F_b(\phi) + \frac{\xi^2}{2}|\nabla\phi|^2\right]d\Omega + \int_{\partial\Omega_S} F_w(\phi)\,ds. \tag{16}$$

Here, $F_b(\phi) = (1-\phi^2)^2/4$ is a double-well potential, and $F_w(\phi)$ is the wall component of the free energy that models fluid/solid (wetting) interactions along the solid surface $\partial\Omega_S$. The parameter $\sigma = (3/2\sqrt{2})\gamma$ is related to the surface tension γ, and ξ is a small parameter controlling the width of the diffuse interface, such that in the limit of $\xi \to 0$, one recovers the macroscopic sharp interface formulation [22–25]. Minimization of the free energy (16) gives

$$\eta = \frac{\sigma}{\xi}[F_b'(\phi) - \xi^2\nabla^2\phi], \tag{17}$$

defined in Ω alongside the natural boundary condition:

$$\sigma\xi(\mathbf{n}\cdot\nabla\phi) = -F_w', \tag{18}$$

which is applied on $\partial\Omega_S$. It is convenient to nondimensionalize Eqs. (15)–(18) by choosing the following dimensionless variables:

$$\mathbf{r}^* = \frac{\mathbf{r}}{L}, \quad \mathbf{u}^* = \frac{\mathbf{u}}{U}, \quad t^* = \frac{Ut}{L}, \quad p^* = \frac{p}{\rho U^2}, \quad \eta^* = \frac{\eta}{\eta_0}, \quad \phi^* = \frac{\phi}{\phi_e}, \tag{19}$$

where L, U, and $\eta_0 = \sigma/L$ are the typical length, velocity, and chemical potential scales of the system, respectively, obtaining

$$\frac{\partial\phi}{\partial t} + \mathbf{u}\cdot\nabla\phi = \frac{1}{\mathrm{Pe}}\nabla^2\eta, \tag{20a}$$

$$\eta = \frac{1}{\mathrm{Cn}}(-\phi + \phi^3 - \mathrm{Cn}^2\nabla^2\phi), \tag{20b}$$

$$\frac{\partial\mathbf{u}}{\partial t} + (\mathbf{u}\cdot\nabla)\mathbf{u} = -\nabla p + \frac{1}{\mathrm{Re}}\nabla^2\mathbf{u} - \frac{1}{\mathrm{We}}\phi\nabla\eta, \tag{20c}$$

alongside the continuity equation $\nabla\cdot\mathbf{u} = 0$. For simplicity, we have dropped the asterisks in the dimensionless variables, and we have taken $\phi_e = 1$. The set of dimensionless parameters in the above equations are defined as

$$\mathrm{Pe} = \frac{UL^2}{M\sigma}, \quad \mathrm{Cn} = \frac{\xi}{L}, \quad \mathrm{Re} = \frac{\rho LU}{\mu}, \quad \mathrm{We} = \frac{\rho U^2 L}{\sigma},$$

which correspond to the Péclet number, Cahn number, Reynolds number, and Weber number, respectively. Following the work reported in Refs. [26,27], the Péclet number is chosen to be inversely proportional to Cn^2 and throughout this study is set to $\mathrm{Pe} = 1/3\mathrm{Cn}^2$. For the other parameters, we take the values of $\mathrm{Re} = 1$, $\mathrm{We} = 0.2$, and $\mathrm{Cn} = 0.01$.

In this formulation we choose F_w to be a linear function in ϕ [28–30], given by $F_w(\phi) = -(\sqrt{2}\sigma/3)\cos\Theta(x)\phi$, where $\Theta(x)$ is the local equilibrium contact angle, which we assume that may depend on the position x. After nondimensionalization, the boundary condition at the solid/fluid wall given by Eq. (18), becomes

$$\mathbf{n}\cdot\nabla\phi| = \frac{\sqrt{2}}{3Cn}\cos\Theta(x). \tag{21}$$

To complete the governing equations we specify boundary conditions at the solid surface and away from the droplet's interface. We impose no-slip boundary conditions along the solid boundary $\partial\Omega_S$ as well as periodic boundary conditions for the velocity and pressure. To drive slow evaporation and dynamically change the size of the droplet, we impose a fixed flux at the top of the system by imposing a von Neumann's boundary condition for the chemical potential:

$$\mathbf{n}\cdot\nabla\eta|_{y=y_w} = -\eta_w, \tag{22}$$

where y_w corresponds to the location of the top boundary, and $\eta_w > 0$ is the imposed value for the chemical potential, noting that for $\eta_w = 0$ the system is closed. As is discussed in Ref. [5], imposing either a fixed flux or a constant value of ϕ at a surface away from the droplet interface is equivalent to imposing a boundary of constant concentration when solving the diffusion equation for the gas vapor concentration. The system of equations and boundary equation conditions is solved by making use of finite elements (see the Appendix).

To validate the numerical model, we first carry out simulations of the equilibrium state of droplets on solid substrates of uniform wetting properties. Figures 5(a) and 5(b) show the equilibrium shapes for a hydrophilic and a hydrophobic homogeneous surface with $\Theta = 70^\circ$ and $\Theta = 110^\circ$, respectively. The contact angle was calculated numerically from the computations and is in excellent agreement with that imposed by condition (21).

We then impose the open flux boundary condition (22) with $\eta_w = 4$ to drive evaporation. Figures 5(c) and 5(d) show the time evolution of the squared lateral radius, $R(t)^2$, and size

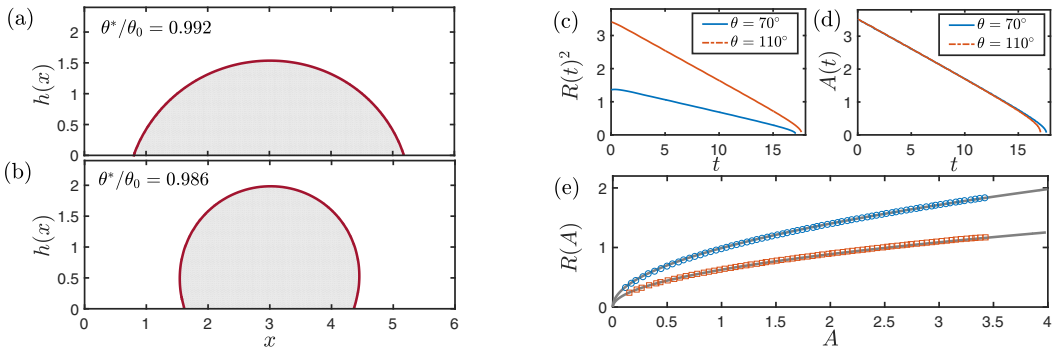

FIG. 5. (a), (b) Equilibrium droplet shapes on homogeneous substrates with different wetting properties. The contact angle imposed by condition (21) is denoted as θ_0 and the angle calculated numerically as θ^*. (c), (d) Time-dependent evolution of the squared droplet lateral radius, $R(t)^2$, and size, $A(t)$, for two different wetting properties. (e) Comparison between the numerically computed droplet lateral radius as function of its size and the theoretical expression given by Eq. (2a) with $\theta = \theta_0$ (solid gray lines). Blue circles and red squares correspond to $\theta_0 = 70^\circ$ and $\theta_0 = 110^\circ$, respectively.

$A(t)$, and show that the droplet's footprint decreases in time as $R(t) \sim t^{1/2}$. Figure 5(e) shows a parametric plot of the instantaneous radius versus cross-sectional area of the droplet. At all times, the simulation data follow the equilibrium geometrical relation given Eq. (2a), hence confirming that the evaporation of the droplet is quasistatic, and that the droplet radius varies with time as $R^2(t) = [2\sin^2\theta_0/(2\theta_0 - \sin 2\theta_0)]A(t)$.

B. Droplet evaporation on symmetric patterns

We first consider a droplet evaporating on a symmetric chemical pattern given by Eq. (1) with $\mathcal{F}(x) = \cos(2\pi x)$ and $\epsilon = 0.1$. The droplet is initially aligned with a maximum of the chemical pattern. We set the evaporation rate to $\eta_w = 2$. Figure 6(a), left panel, shows that, as the droplet size decreases quasistatically, the evolution of the lateral radius $R(A)$ is in excellent agreement with the trajectory predicted by the theoretical bifurcation diagram (shown with gray lines).

For droplet sizes larger than the critical value A_p, which marks the onset of a pitchfork bifurcation, the droplet is fully stable and aligns with the maximum of the chemical pattern. When

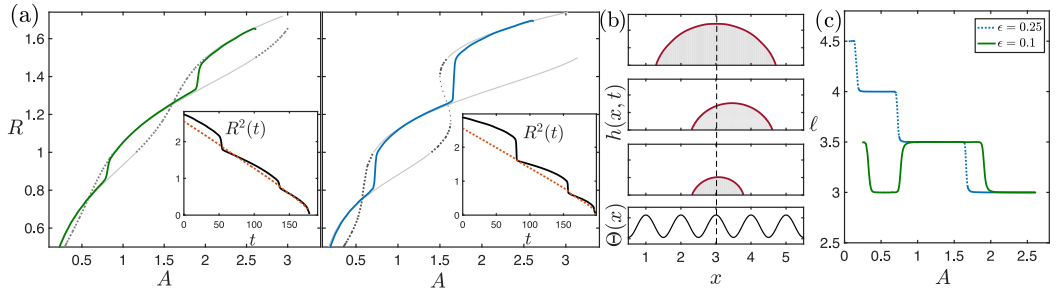

FIG. 6. Numerical simulations of slow evaporation by solving the CH-NS system of equations, Eqs. (20), with a symmetric chemical pattern, and with an evaporation rate of $\eta_w = 2$. (a) Solid lines show the time evolution of the droplet footprint as function of the droplet size for $\epsilon = 0.1$ (left) and $\epsilon = 0.25$ (right). The underlying gray lines correspond to the theoretical bifurcation diagrams shown in Fig. 2. The solid lines of the inlet panels show the time evolution of $R^2(t)$, and the red dotted lines show the evolution of $[2\sin^2\theta_0/(2\theta_0 - \sin 2\theta_0)]A(t)$. Panel (b) shows droplet snapshots at different times, and panel (c) shows the evolution of the droplet's midpoint as a function of the droplet size. In all cases $\theta_0 = 70^\circ$.

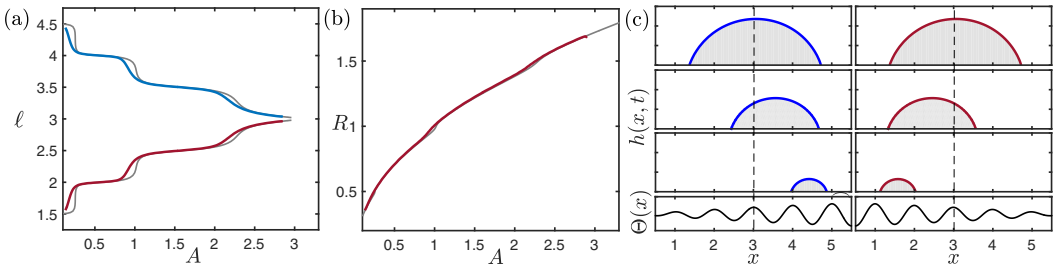

FIG. 7. Numerical simulations of the CH-NS system of equations, Eqs. (20), with a chemical pattern given by Eq. (14) with $\epsilon = 0.1$ and $L = 6$. Panel (a) shows the evolution of the droplet's midpoint as function of its size for a positive gradient (blue solid line) and negative gradient (red solid line). The underlying gray lines correspond to the stable solutions predicted by the theory. Panel (b) shows the droplet's footprint versus its size (red solid line) compared to the theoretical prediction (gray line). Panels in (c) show the corresponding droplet profiles at different times.

$A < A_p$, the droplet solution becomes unstable against asymmetric perturbations, and any small perturbation (in the present case, numerical noise) is able to break the plane symmetry forcing the droplet to shift laterally to a stable branch of solutions, which are aligned with a minimum of the chemical pattern and are located either to the left or right of the droplet's original location ($\ell = 3$) [see Fig. 6(b)]. The droplet then continues following the bifurcation diagram in this new location until another pitchfork bifurcation occurs, forcing the droplet to shift and to be aligned with a maximum again. The inlet panels of Fig. 6(a) show the time evolution of $R^2(t)$, where we can see that it smoothly and continuously decreases over time, except at the pitchfork bifurcation points, when an abrupt step change is observed. The red dotted line corresponds to the linear behavior that would be expected on a homogeneous surface with contact angle θ_0, which is given by $R^2(t) = [2\sin^2\theta_0/(2\theta_0 - \sin 2\theta_0)]A(t)$. We can see that only for long times (i.e., small droplet sizes), both curves converge to the same point. These results show that the contact line motion is not affected by pinning and depinning mechanisms but by the underlying bifurcation sequence that is induced by the wetting pattern.

The trajectory of droplet's midpoint as a function of its size is shown in Fig. 6(c), where we can see that lateral movements occur over a much faster timescale than the timescale of evaporation [see also the inlet panels of Fig. 6(a)]. We note that a similar behavior is observed for larger values of the strength of the chemical pattern [see Figs. 6(a) and 6(c) for $\epsilon = 0.25$ and Supplemental Movie 1 [31]]. Such fast lateral movements correspond to the snap events that have been reported on topographical smooth surfaces [17], where the same behavior was observed [e.g., compare the evolution of $R^2(t)$ for $\epsilon = 0.25$ in Fig. 6(a) with the results shown in Fig. 1(d) of Ref. [17]]. This indicates that both smooth wetting patterns and smooth topographies lead to the same type of dynamics. It is important to remark that, because of the symmetry of the chemical pattern, the direction taken by the droplet at each pitchfork bifurcation is not predictable and hence cannot be controlled, i.e., the droplet can shift either to the right or to the left.

C. Droplet evaporation on asymmetric patterns

In this section we study the evaporation of a droplet on an asymmetric pattern. We impose a chemical pattern with an amplitude gradient, described by Eq. (14), where the amplitude of the chemical pattern gradually increases or decreases with x. Figure 7(a) shows the trajectories of the droplet's midpoint as the droplet size decreases for the case with a positive gradient (blue solid line) and negative gradient (red solid line). We observe that in both cases, the asymmetry of the chemical pattern induces a continuous change in the droplet's midpoint location, forcing the droplet to move either to the left or right as its size decreases in time.

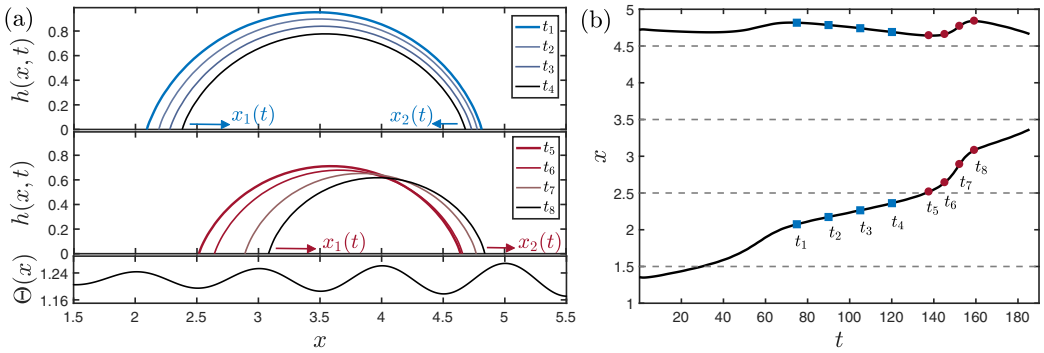

FIG. 8. (a) Droplet profiles at different times of the numerical simulations shown in the left panel of Fig. 7(c). Numerical times are $t_1 = 75, t_2 = 90, t_3 = 105, t_4 = 115, t_5 = 138, t_6 = 145, t_7 = 152$, and $t_8 = 159$. The bottom graph shows the asymmetric chemical pattern. Panel (b) shows the evolution of the droplet's contact points, $x_1(t)$ (bottom curve) and $x_2(t)$ (top curve). The times shown in panel (a) are marked with solid squares and circles for reference. Dashed lines denote the location of the minima of the wetting pattern.

We note that, as predicted by the theoretical analysis shown in Fig. 7, the bifurcation diagrams for this type of chemical patterns consists of a series of disconnected branches, which are either stable or saddle node. If the droplet is initially located at a stable location, it will remain on this branch during the entire process and continuously move following the stable branch of solutions, as is observed in Fig. 7(a). It is worth noting that in both cases of the gradient sign the droplet's footprint decreases continuously in time following the same trajectory on the (A, R) plane, as predicted by the theory [see Fig. 7(b)].

Counterintuitively, it is seen that the droplet moves towards higher amplitude of the chemical pattern, moving to the right with positive gradient and to the left with negative gradient; see Fig. 7(c) and Supplemental Movies 2A and 2B [31]. Such behavior can be understood by tracking the dynamics of the droplet's contact points, $x_1(t)$ and $x_2(t)$. Figure 8 shows the time evolution of the droplet's profile and contact points, where we distinguish between two dynamic stages.

In a first stage both contact points move in opposite directions towards a minimum of the wetting pattern [see top panel of Fig. 8(a) and squared blue points in Fig. 8(b)]. As the droplet evaporates quasistatically both contact angles remain the same while the contact points $x_1(t)$ and $x_2(t)$ slowly recede in time. Hence, over a time interval Δt, the contact points will have moved a distance Δx_1 and Δx_2 while the change in contact angle $\Delta\theta$ is the same at both points. On symmetric patterns the local gradient of the wetting pattern, $m = \Delta\Theta/\Delta x$, has the same magnitude on both contact points and so $|\Delta x_1| = |\Delta x_2|$, and hence the droplet remains aligned with either a minimum or maximum of the chemical pattern until a snap occurs [cf. Fig. 6(c)]. However, on asymmetric patterns, the local gradient is different at each contact point, say, m_1 and m_2, leading to different lateral displacements: $\Delta x_1 = (m_2/m_1)\Delta x_2$. A chemical pattern with a positive gradient has $|m_1| < |m_2|$, so $|\Delta x_1| > |\Delta x_2|$ and the droplet overall moves to the right, as observed numerically. If the gradient is negative, the opposite behavior is observed.

When the left contact point $x_1(t)$ reaches the minimum of the chemical pattern located around $x = 2.5$ [see Fig. 8(a)] a different dynamic behavior is observed, in which the right contact point x_2 starts to move to the right in the same direction as x_1 (see t_5–t_8 in Fig. 8). This is a consequence of the amplitude gradient of the wetting pattern, and in particular of the difference between its minimum values. Let Θ_1 and Θ_2 be the minima located at around $x = 2.5$ and $x = 4.5$, respectively. As $x_1(t)$ passes through Θ_1 and $x_2(t)$ approaches Θ_2, because $\Theta_1 > \Theta_2$ there is an energy barrier that prevents x_2 to move further to the left. Therefore, both contact points can only move to the right as the droplet evaporates. (And the opposite behavior is observed with a negative amplitude gradient.)

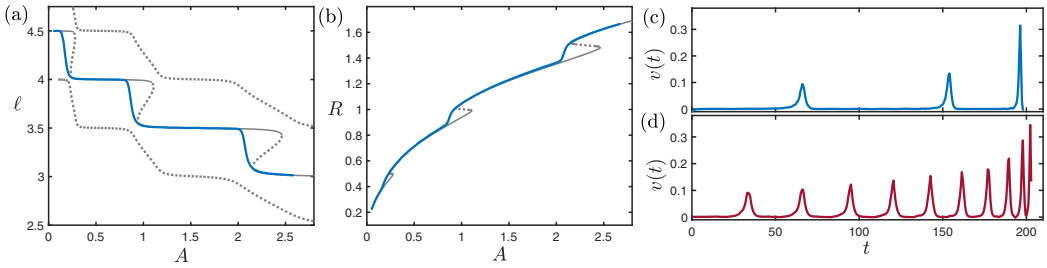

FIG. 9. Numerical simulations of the CH-NS system of equations, Eqs. (20), a chemical pattern given by Eq. (14) with $\epsilon = 0.1$ and $L = 0.6$. Panel (a) shows the evolution of the droplet's midpoint as function of its size and the underlying gray lines correspond to the stable solutions predicted by the theory. Panel (b) shows the droplet's footprint versus its size (blue solid line) compared to the theoretical prediction (gray line). Panel (c) shows the speed $v(t)$ of the droplet's midpoint versus time (dashed blue line). Panel (d) shows the same speed but for a chemical pattern with smaller wavelength λ. In all cases $\theta_0 = 70^\circ$.

By setting $L = 0.6$ and keeping the same numerical domain size we approach the limit described in Sec. II B [Fig. 4(c)] in which the chemical pattern is nearly symmetric. Figures 9(a) and 9(b) show the trajectories of the droplet's midpoint and footprint as function of the droplet size, respectively. We can recognize the presence of turning points on the $\ell(A)$ trajectory [see gray lines in Fig. 9(a)] leading to a rapid change in both the droplet's midpoint and footprint, similar to the snap events observed under symmetric patterns. However, because there is now a symmetry breaking the change in droplet's location is induced by imperfect pitchfork bifurcations. Hence, all movements are directed towards the same direction allowing for a better control of droplet's position.

The presence of snap events is clearly demonstrated in Fig. 9(c), where we plot the speed of the droplet's midpoint, $v(t) = \dot{\ell}(t)$. We can see that droplet's lateral movements become faster as the droplet size decreases. Decreasing the wavelength of the chemical pattern (but keeping the same initial droplet size, i.e., effectively increasing the dimensionless variable A) leads to a dynamics with a higher rate of lateral shifts [see Fig. 9(d) and Supplemental Movies 3 and 4 [31]]. This shows that the theoretical basis in terms of bifurcations is still valid in this case.

IV. CONCLUDING REMARKS

We have presented analytical and computational results on quasistatic evaporation of a 2D droplet on a flat, chemically patterned surface. We considered patterns that are pinning free but have a smooth and periodic variation of the local equilibrium contact angle. We have shown that symmetric patterns lead to a hierarchy of bifurcations in the 3D parameter space represented by the droplet's cross-sectional area, midpoint, and footprint. For an amplitude ϵ of the chemical pattern smaller than a critical value ϵ_c the nodes of the network correspond to pitchfork bifurcations that mark transitions between stable and saddle points. For $\epsilon > \epsilon_c$ a cusp bifurcation occurs leading to multiplicity of solutions and the emergence of turning points that mark the onset of saddle-node bifurcations. A summary of all bifurcations is presented in Table I.

A detailed bifurcation analysis has revealed that pitchfork bifurcations occur at well defined locations of the chemical pattern, which are independent of the homogeneous contact angle and amplitude of the chemical variation. We have also shown that the amplitude critical value scales with the droplet's size as $\epsilon_c \sim A_c^{-1/2}$, hence suggesting that cusp bifurcations are favored in the microscopic limit. Introducing a bias in the chemical pattern leads to a topological change in the bifurcation diagrams, whereby equilibrium solutions are characterized by disconnected branches in the parameter space. Such branches, which can be either stable or saddle points, are continuously parametrized by the droplet's midpoint, i.e., $\ell(A)$, implying that changing the droplet's size may lead to a continuous lateral displacement.

TABLE I. Summary of all bifurcations analyzed in this work with their associated mathematical prediction, given in terms of the contact radius R_p for the pitchfork bifurcation, the critical amplitude ϵ_c for the cusp bifurcation, and the contact radius R_s for the saddle-node bifurcation. The functions $\beta(\theta_0)$ and $g(x)$ are defined in Eqs. (9) and (11), respectively. The rightmost column describes the physical consequence of each bifurcation.

Bifurcation	Analytical prediction		Physical consequence
Pitchfork	$R_p = n/2$	$(\epsilon \neq 0)$	Symmetry-breaking snap
Cusp	$\epsilon_c \sim \beta(\theta_0) A_c^{-1/2}$	$(\epsilon = \epsilon_c)$	Multiplicity of solutions
Saddle-node	$g(2\pi R_s) = \beta(\theta_0)/\epsilon$	$(\epsilon > \epsilon_c)$	No symmetry-breaking snap

We have studied droplet dynamics upon evaporation by making use of the Cahn-Hilliard and Navier-Stokes system of equations. Periodic and symmetric patterns lead to a sequence of events where the droplet exhibits rapid lateral movements when its cross-sectional area reaches the pitchfork bifurcations predicted by the theory, which mark a transition from a stable state to a saddle node. As a consequence of numerical noise the droplet's plane symmetry can be broken, hence triggering lateral motion via a symmetry-breaking snap. It is important to note that if the plane symmetry was not broken, the pitchfork bifurcation could be bypassed hence leading to a snap with no symmetry breaking, whereby the droplet would remain on the same location while its radius undergoes a rapid change. Our results show that the *snap evaporation* reported on nonplanar symmetric substrates [17] is also observed on planar surfaces with symmetric chemical patterns, and in both cases, this is a consequence of a hierarchy of pitchfork and saddle-node bifurcations.

In asymmetrical chemical patterns, the presence of disconnected branches leads to a smooth droplet's motion where its location continuously changes towards one direction, hence showing that droplet's motion can be controlled upon evaporation. We have established that this is a consequence of the local gradient of the wetting pattern, which is different on each contact point, and the difference between minima of the chemical pattern. Such bias leads to an effective droplet's lateral motion towards regions of higher amplitude. In the limit of weak bias, the droplet dynamics is characterized by snap events, but because of the slight symmetry breaking of the chemical pattern, they always occur towards the same direction. We have also shown that the maximum droplet's speed during a snap event increases as the droplet's size decreases.

The ideas presented here can be used in applications of droplet control and mass transport. We have shown that well-designed chemical patterns can lead to a well-controlled motion of the droplet as its size changes in time. The mechanism that controls the snap dynamics is the conversion of surface energy into motion, which involves kinetic energy and energy dissipation, and our numerical results show that during a snap the droplet always covers half a wavelength of the underlying chemical pattern. Here we have studied situations where the droplet transitions between adjacent loci in the chemical pattern, and thus the motion of the droplet is controlled by the periodicity of the pattern and the size of the droplet. However, by studying the effect of inertia, it is possible that the droplet undergoes translations over more than one period of the underlying pattern. This is an open question that we intend to address in the future. In addition, there are a number of ways of extending the work reported here, for example, including gravitational effects, considering different types of periodic patterns, or extending the analysis to 3D systems. It is also important to note that we have focused on evaporation, but our analysis is equally applicable to other physical processes, such as condensation or mass transfer. We intend to address these and related issues in future studies.

ACKNOWLEDGMENTS

We are grateful to Dr. Matthew Haynes from the School of Mathematics and Statistics at the Open University for useful discussions. We acknowledge financial support by the UK Engineering and Physical Sciences Research Council (EPSRC) through Grant No. EP/R041954/1.

APPENDIX: NUMERICAL METHOD

The system of the Cahn-Hilliard and Navier-Stokes equations, Eqs. (20a)–(20c), is solved using finite elements. To this end, these equations are expressed in variational form (weak formulation), which is obtained by multiplying each equation by test functions that are the basis of unknown functions to be approximated, called trial functions, and integrating the resulting equation over the domain Ω.

To obtain the weak formulation of the system (20a)–(20c), we define test functions $(\Phi, \Psi, \boldsymbol{\Xi}, \Pi) \in H^1(\Omega) \times H^1(\Omega) \times W \times L^2(\Omega)$ corresponding to the trial functions $(\phi, \eta, \mathbf{u}, p)$, where W is defined as

$$W = \{\mathbf{v} \in H^1(\Omega) \times H^1(\Omega) : \mathbf{v} = 0 \ \text{ on } \ \partial\Omega\},$$

and Ω, $\partial\Omega$, $L^2(\Omega)$, and $H^1(\Omega)$ are the spatial domain, boundary of Ω, the space of twice integrable functions, and the Sobolev space, respectively. We first consider the Cahn-Hilliard equation by multiplying Eqs. (20a) and (20b) by Φ and Ψ, respectively, and integrating over the whole domain Ω, to obtain

$$\left\langle \frac{\partial \phi}{\partial t}, \Phi \right\rangle + \langle \mathbf{u}\cdot\nabla\phi, \Phi\rangle + \frac{1}{\mathrm{Pe}}\langle \nabla\eta, \nabla\Phi\rangle - \frac{1}{\mathrm{Pe}}\langle \mathbf{n}\cdot\nabla\eta, \Phi\rangle_{\partial\Omega} = 0, \tag{A1}$$

$$\langle \eta, \Psi\rangle + \left\langle \left(\frac{\phi - \phi^3}{\mathrm{Cn}}\right), \Psi \right\rangle - \mathrm{Cn}\langle \nabla\phi, \nabla\Psi\rangle + \mathrm{Cn}\langle \mathbf{n}\cdot\nabla\phi, \Psi\rangle_{\partial\Omega} = 0, \tag{A2}$$

where $\langle\cdot,\cdot\rangle$ denotes the $L^2(\Omega)$ inner product. The Cahn-Hilliard equation (A1)–(A2) is discretized in time using the Crank-Nicolson scheme. The Navier-Stokes equation is solved by adopting Chorin's method [32] where we first ignore the pressure in Eq. (20c), which is then discretized in time using the backwards finite difference method to compute the tentative velocity $\mathbf{u}_T$:

$$\frac{\mathbf{u}_T - \mathbf{u}^{n-1}}{\delta t_n} + \mathbf{u}^{n-1}\cdot\nabla\mathbf{u}^{n-1} = \frac{1}{\mathrm{Re}}\nabla^2\mathbf{u}^{n-1} - \frac{1}{\mathrm{We}}\phi^n\nabla\eta^n, \tag{A3}$$

where δt_n is the time step and $\mathbf{u}^n$ is the value of $\mathbf{u}$ at time t_n. This is corrected to obtain the final velocity $\mathbf{u}^n$ as

$$\frac{\mathbf{u}^n - \mathbf{u}_T}{\delta t_n} = -\nabla p^n. \tag{A4}$$

The pressure p^n at time t^n is computed by taking the divergence of Eq. (A4) and using the continuity equation

$$\frac{\nabla\cdot\mathbf{u}_T}{\delta t_n} = \nabla^2 p^n. \tag{A5}$$

Finally, the weak form of the Navier-Stokes equation (20c) is obtained by multiplying both Eqs. (A3) and (A4) by $\boldsymbol{\Xi}$ and Eq. (A5) by Π. Integrating over the Ω we then compute the tentative velocity $\mathbf{u}_T$, pressure p^n, and velocity $\mathbf{u}^n$ at time $t = t_n$:

$$\left\langle \frac{\mathbf{u}_T - \mathbf{u}^{n-1}}{\delta t_n}, \boldsymbol{\Xi} \right\rangle + \langle \mathbf{u}^{n-1}\cdot\nabla\mathbf{u}^{n-1}, \boldsymbol{\Xi}\rangle + \frac{1}{\mathrm{Re}}\langle \nabla\mathbf{u}^{n-1} : \nabla\boldsymbol{\Xi}\rangle = -\frac{1}{\mathrm{We}}\langle \phi^n\nabla\eta^n, \boldsymbol{\Xi}\rangle, \tag{A6}$$

$$\langle \nabla p^n, \nabla\Pi\rangle = -\frac{1}{\delta t_n}\langle \nabla\cdot\mathbf{u}_T, \Pi\rangle, \tag{A7}$$

$$\langle \mathbf{u}^n, \boldsymbol{\Xi}\rangle = \langle \mathbf{u}_T, \boldsymbol{\Xi}\rangle - \delta t_n\langle \nabla p^n, \boldsymbol{\Xi}\rangle, \tag{A8}$$

where $\langle\cdot : \cdot\rangle$ denotes the vector inner product.

[1] D. Brutin and V. Starov, Recent advances in droplet wetting and evaporation, Chem. Soc. Rev. **47**, 558 (2018).
[2] R. Picknett and R. Bexon, The evaporation of sessile or pendant drops in still air, J. Colloid Interface Sci. **61**, 336 (1977).
[3] R. Deegan, O. Bakajin, T. F. Dupont, G. Huber, S. R. Nagel, and A. Witten, Capillary flow as the cause of ring stains from dried liquid drops, Nature (London) **389**, 827 (1997).
[4] H. Hu and R. G. Larson, Evaporation of a sessile droplet on a substrate, J. Phys. Chem. B **106**, 1334 (2002).
[5] R. Ledesma-Aguilar, D. Vella, and J. Yeomans, Lattice-Boltzmann simulations of droplet evaporation, Soft Matter **10**, 8267 (2014).
[6] J. M. Stauber, S. K. Wilson, B. R. Duffy, and K. Sefiane, On the lifetimes of evaporating droplets, J. Fluid Mech. **744**, R2 (2014).
[7] E. Dietrich, E. S. Kooij, X. Zhang, H. J. Zandvliet, and D. Lohse, Stick-jump mode in surface droplet dissolution, Langmuir **31**, 4696 (2016).
[8] P. Sáenz, A. Wray, Z. Che, O. Matar, P. Valluri, J. Kim, and K. Sefiane, Dynamics and universal scaling law in geometrically-controlled sessile drop evaporation, Nat. Commun. **8**, 14783 (2017).
[9] A. Amini and G. M. Homsy, Evaporation of liquid droplets on solid substrates. II. Periodic substrate with pinned or moving contact line, Phys. Rev. Fluids **2**, 043604 (2017).
[10] A. W. Wray, B. R. Duffy, and S. K. Wilson, Competitive evaporation of multiple sessile droplets, J. Fluid Mech. **884**, A45 (2020).
[11] T. Wong, S. H. Kang, S. K. Y. Tang, E. J. Smythe, B. D. Hatton, A. Grinthal, and J. Aizenberg, Bioinspired self-repairing slippery surfaces with pressure-stable omniphobicity, Nature (London) **477**, 443 (2011).
[12] J. D. Smith, R. Dhiman, S. Anand, E. Reza-Garduno, R. E. Cohen, G. H. McKinley, and K. K. Varanasi, Droplet mobility on lubricant-impregnated surfaces, Soft Matter **9**, 1772 (2013).
[13] J. H. Guan, É. Ruiz-Gutiérrez, B. B. Xu, D. Wood, G. McHale, R. Ledesma-Aguilar, and G. G. Wells, Drop transport and positioning on lubricant-impregnated surfaces, Soft Matter **13**, 3404 (2017).
[14] L. Wang and T. J. McCarthy, Covalently attached liquids: Instant omniphobic surfaces with unprecedented repellency, Angew. Chem. Int. Ed. **55**, 244 (2016).
[15] J. H. Guan, G. G. Wells, B. Xu, G. McHale, D. Wood, J. Martin, and S. Stuart-Cole, Evaporation of sessile droplets on slippery liquid-infused porous surfaces (slips), Langmuir **31**, 11781 (2015).
[16] S. Armstrong, G. McHale, R. Ledesma-Aguilar, and G. G. Wells, Pinning-free evaporation of sessile droplets of water from solid surfaces, Langmuir **35**, 2989 (2019).
[17] G. G. Wells, E. Ruiz-Gutierrez, Y. L. Lirzin, A. Nourry, B. V. Orme, M. Pradas, and R. Ledesma-Aguilar, Snap evaporation of droplets on smooth topographies, Nat. Commun. **9**, 1380 (2018).
[18] H. Barrio-Zhang, E. Ruiz-Gutiérrez, S. Armstrong, G. McHale, G. G. Wells, and R. Ledesma-Aguilar, Contact-angle hysteresis and contact-line friction on slippery liquid-like surfaces, Langmuir **36**, 15094 (2020).
[19] M. S. Salludah, G. Launay, J. Parle, R. Ledesma-Aguilar, Y. Gizaw, G. McHale, and G. G. Wells, Bidirectional motion of droplets on gradient liquid infused surfaces, Commun. Phys. **3**, 166 (2020).
[20] M. Pradas, N. Savva, J. Benziger, I. Kevrekidis, and S. Kalliadasis, Dynamics of fattening and thinning 2D sessile droplets, Langmuir **32**, 4736 (2016).
[21] S. Strogatz, *Nonlinear Dynamics and Chaos* (Addison-Wesley, New York, 1985).
[22] P. Seppecher, Moving contact lines in the Cahn-Hilliard theory, Int. J. Eng. Sci. **34**, 977 (1996).
[23] D. Anderson, G. McFadden, and A. Wheeler, Diffuse-interface methods in fluid mechanics, Annu. Rev. Fluid Mech. **30**, 139 (1998).
[24] P. Yue, C. Zhou, and J. Feng, Sharp-interface limit of the Cahn-Hilliard model for moving contact lines, J. Fluid Mech. **645**, 279 (2010).
[25] D. Sibley, A. Nold, and S. Kalliadasis, Unifying binary fluid diffuse-interface models in the sharp-interface limit, J. Fluid Mech. **736**, 5 (2013).
[26] H. Ding, P. D. M. Spelt, and C. Shu, Diffuse interface model for incompressible two-phase flows with large density ratios, J. Comput. Phys. **226**, 2078 (2007).

[27] F. Magaletti, F. Picano, M. Chinappi, L. Marino, and C. M. Casciola, The sharp-interface limit of the Cahn-Hilliard/Navier-Stokes model for binary fluids, J. Fluid Mech. **714**, 95 (2013).
[28] J. W. Cahn, Critical point wetting, J. Chem. Phys. **66**, 3667 (1977).
[29] P. G. de Gennes, Wetting: Statics and dynamics, Rev. Mod. Phys. **57**, 827 (1985).
[30] B. Aymard, U. Vaes, M. Pradas, and S. Kalliadasis, A linear, second-order, energy stable, fully adaptive finite element method for phase-field modeling of wetting phenomena, J. Comp. Phys. X **2**, 100010 (2019).
[31] See Supplemental Material at http://link.aps.org/supplemental/10.1103/PhysRevFluids.xx.xxxxxx for [give brief description of material].
[32] A. J. Chorin, Numerical solution of the Navier-Stokes equations, Math. Comp **22**, 745 (1968).